Journal of
Materials Chemistry A

ROYAL SOCIETY
OF CHEMISTRY

PAPER

View Article Online
View Journal

Check for updates

Cite this: DOI: 10.1039/d5ta09769j

Tuning product selectivity in direct electroreduction of NO *via* phase engineering of MoS_2 nanosheets in a water-fed PEM electrolyzer

Min Li,[ac] Frank Hernandez Baena,[a] Shota Matsuo,[a] Mingliang Chen,[a] Boaz Izelaar,[bc] Ruud Kortlever[bc] and Atsushi Urakawa *[ac]

Received 29th November 2025
Accepted 14th April 2026

DOI: 10.1039/d5ta09769j

rsc.li/materials-a

Electrochemical conversion of NO from gaseous pollutants into ammonia using abundant and cost-effective catalyst materials holds great promise for pollutant abatement and for advancing a more closed, sustainable nitrogen cycle. However, regulating product selectivity remains challenging because NO reduction involves complex multielectron/proton pathways. Here, we report two different crystal phases of MoS_2 (2H and 1T′) exhibiting prominent activity in the electrochemical NO reduction reaction (NORR), but showing different selectivities. The faradaic efficiency of ammonia reaches 86% over 2H-MoS_2, outperforming 1T′-MoS_2 (31%) at 2.1 V. In contrast, 1T′-MoS_2 displays higher selectivity towards N_2, especially at a lower cell voltage (50% at 1.7 V). Kinetic and spectroscopic analyses further suggest phase-dependent rate-control characteristics, consistent with distinct pathway preferences on 1T′ *versus* 2H. Overall, these results demonstrate that NORR activity and selectivity can be efficiently tuned by choosing the appropriate MoS_2 phase, providing a simple strategy to tune product selectivity in complex multistep reactions.

Introduction

Nitrogen, the fifth most abundant element on earth, plays an essential role as macronutrient for all living organisms.[1] Within the global nitrogen cycle, various inorganic nitrogenous compounds, including ammonia (NH_3), hydroxylamine (NH_2OH), hydrazine (N_2H_4), nitrous oxide (N_2O), nitric oxide (NO), nitrogen dioxide (NO_2), nitrite (NO_2^-), and nitrate (NO_3^-) are produced in significant quantities by industrial chemical processes.[2] Many of these species, notably NO_x (NO, NO_2 and N_2O) are prominent environmental pollutants. Consequently, mitigating NO_x emissions from fossil fuel combustion, such as power plants and automotive engines, represents a critical focus within nitrogen chemistry.[3] Among these pollutants, NO typically constitutes approximately 95% of NO_x in flue gas.[4]

Conventional selective catalytic reduction (SCR) methods effectively convert NO into harmless dinitrogen gas (N_2).[5] However, SCR requires the input of reducing agents such as NH_3 or H_2, imposing additional energy and material demands.[6] NH_3 itself holds significant importance in agriculture and has recently emerged as a potential H_2 energy carrier.[7,8] Its industrial production is primarily achieved through the Haber–Bosch process, a thermochemically intensive reaction that operates at high pressure (150–300 bar) and temperature (400–500 °C). This process accounts for approximately 1–2% of global energy consumption and 1–1.5% of global CO_2 emissions annually.[9]

Thus, electrochemical approaches for the NO reduction reaction (NORR) offer a promising alternative for both NO abatement and NH_3 synthesis, thereby contributing to a more sustainable nitrogen cycle.[10,11] In particular, the NORR presents thermodynamic advantages: the standard reduction potential of NO to NH_3 (0.71 V *vs.* RHE) is significantly more positive than that of the nitrogen reduction reaction (NRR, 0.093 V *vs.* RHE)[12] and hydrogen evolution reaction (HER), theoretically implying a more favourable reaction path.[13,14] Nonetheless, the practical implementation of the NORR has been hindered by the low solubility of NO in aqueous media (1.92 mmol L^{-1} atm^{-1} at 25 °C), which limits its availability at the electrode surface.[15] Therefore, utilizing membrane electrode assembly (MEA) configurations, more specifically in a proton exchange membrane (PEM) electrolyzer allows direct gaseous NORR, which improves control over the reaction environment and reduces internal resistance. Beyond the traditional H-cell configuration, a PEM electrolyzer facilitates more controlled reagent flow and reaction kinetics, making it attractive for future electrochemical NO conversion technologies (Fig. S1).[16,17]

To date, significant advances have been made in the development of catalytic materials for the NORR, including pure

---

[a] *Department of Chemical Engineering, Delft University of Technology, Van der Maasweg 9, 2629 HZ, Delft, the Netherlands. E-mail: a.urakawa@tudelft.nl*

[b] *Department of Process & Energy, Delft University of Technology, Leeghwaterstraat 39, 2628 CB, Delft, the Netherlands*

[c] *e-Refinery Institute, Delft University of Technology, Leeghwaterstraat 39, 2628 CB Delft, the Netherlands*

transition metals (TMs)[18] noble metals,[19] alloys,[20] metal oxides[21] and single-atom catalysts (SACs).[22] Nonetheless, challenges still remain due to the low abundance and thus high costs associated with noble metals, the limited activity of pure TMs, and the insufficient long-term stability of SACs, emphasizing the need to design cost-effective, efficient, and durable electrocatalysts for denitrification.[23] Within the family of transition metal dichalcogenides (TMDs), monolayer molybdenum disulfide (MoS_2) is a widely studied, earth-abundant and low-cost electrocatalyst that has demonstrated excellent HER performance.[24] Compared to the commonly studied semiconducting 2H phase, MoS_2 in its octahedral (1T) or distorted octahedral (1T′) configurations has shown superior catalytic activity for the HER.[25] A key advantage of TMDs is the tunability of their atomic-scale structure, which offers opportunities to adjust the selectivity of multielectron/proton reactions.[26] In this context, exploring phase-dependent electrocatalytic activity is vital to achieve a deeper understanding of the origins of catalytic performance. Nakamura *et al.*[27] identified a Mo(V) intermediate unique to 1T-MoS_2 that promotes N–N coupling selectivity by decoupling proton and electron transfer to the sequential proton–electron transfer (SPET) pathway. In contrast, 2H-MoS_2 favours NH_3 production during NO_3^- reduction *via* the concerted proton–electron transfer (CPET) pathway. Similarly, Yu *et al.*[28] investigated the reaction at near-neutral pH, reporting that the strong hydrogen affinity and favourable hydrogenation of nitrogenous intermediates on 1T-MoS_2 make this phase particularly promising for NO_3^- to NH_3 conversion. However, these studies have primarily focused on liquid-phase nitrate reduction under mild pH conditions (pH 4–7) in three-electrode cell configurations. Therefore, the role of MoS_2 crystal phases in direct gas-phase NO reduction under acidic conditions in industrially relevant PEM electrolyzers remains insufficiently understood and requires further investigation.

In this work, we explored phase-engineered MoS_2 nanosheets (2H and 1T′) as effective catalysts for direct gaseous NO electroreduction in a PEM electrolyzer, enabling a pronounced and controllable selectivity switch between NH_3 and N_2. 2H-MoS_2 achieved a high NH_3 yield of 558 μmol cm^{-2} h^{-1} at 2.3 V and the highest FE of 86% at 2.1 V, exceeding the performance of the 1T′ phase. Notably, the 1T′ phase-dominant MoS_2 demonstrated greater selectivity for N–N coupling products (N_2), particularly under low applied potentials, and 50% FE towards N_2 at 1.7 V. To uncover the origin of this phase-dependent selectivity, we establish a mechanistic picture by integrating LSV with local Tafel/derivative analysis, an apparent kinetic isotope effect, and *ex situ* NO-DRIFTS, revealing distinct apparent rate-control characteristics on 2H *versus* 1T′, and thus we connect the stronger NO-derived adsorption signatures of 1T′ to coverage-enabled N–N coupling, whereas the pronounced apparent KIE on 2H supports a proton-coupled hydrogenation contribution consistent with enhanced NH_3 selectivity. Overall, these findings highlight phase engineering of TMD catalysts as a practical strategy to tune product selectivity in complex multistep proton–electron transfer reactions.

Results and discussion

Material synthesis and characterization

The 2H-MoS_2 (trigonal phase) material was successfully synthesized using a one-step hydrothermal method as illustrated in Fig. S2(a).[29] Meanwhile, distorted 1T′-MoS_2 (octahedral phase) was obtained by adding hydrazine monohydrate ($N_2H_4 \cdot H_2O$) during the synthesis, as depicted schematically in Fig. S2(b).[29] XRD patterns of the as-prepared samples are shown in Fig. 1(a). For the synthesized 2H-MoS_2, the (002) peak located at 13.9° shifted slightly towards a lower angle compared to that of 14.4° in highly crystalline 2H-MoS_2 (JCPDS Card no. 73-1508). This was ascribed to the interlayer stress as a result of disordered structures.[30] The calculated interlayer distance of the synthesized 2H-MoS_2 is 0.62 nm, originating from the interference among the 2H-MoS_2 layers along the *c*-axis. At higher angles, the appearance of the (100) and (110) peaks in the 2H-MoS_2 sample (hereafter referred to as 2H-MoS_2) indicated the same basal plane orientation with highly crystalline 2H-MoS_2. For the synthesized 1T′-MoS_2 sample (hereafter referred to as 1T′-MoS_2), the (002) peak is drastically shifted to 9.2° compared to the peak of 2H-MoS_2, which indicates lattice expansion as the interlayers are intercalated with N_2H_4.[31] According to the Bragg equation, the corresponding interlayer distances of the peaks were 0.93 nm and 0.49 nm at 9.2° and 18.2°, respectively.[32] The broad XRD diffraction peak can be an indication of the coexistence of both 2H and 1T′ phases in the hydrazine intercalated 1T′ sample.[33] Scanning electron microscopy (SEM) images of the prepared 2H and 1T′ MoS_2 samples are shown in Fig. 1(b and c). Both pictures show nano-flowers consisting of small, intersecting nanosheets. This morphology is characterized by short lateral dimensions and a lack of extended stacking, which geometrically necessitates a high density of exposed edge S atoms which are the active sites, compared to flat for bulk 2H-

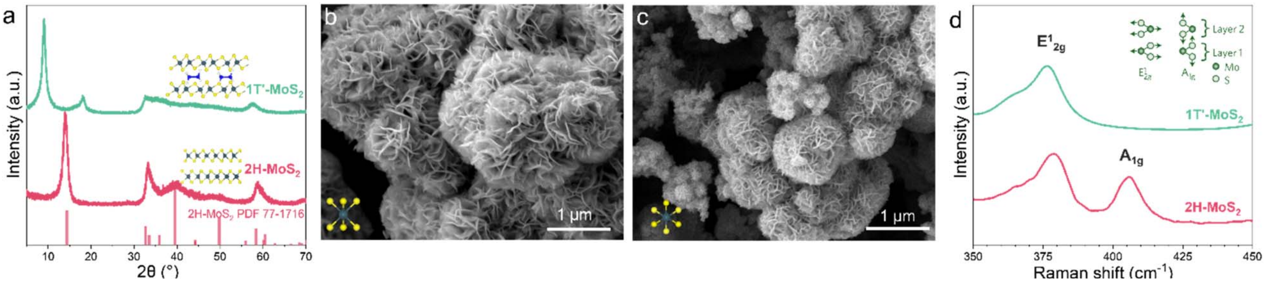

Fig. 1 (a) XRD patterns of 2H- and 1T′-MoS_2; (b and c) SEM images of 2H- and 1T′-MoS_2; (d) Raman spectra of 2H- and 1T′-MoS_2.

MoS_2. The disordered arrangement of these nanosheets prevents the van der Waals restacking of typical bulk crystals, thereby maximizing the accessible surface area and defect density.[34]

Fig. 1(d) presents Raman spectra of the synthesized 2H and 1T′ phase MoS_2 nanoflowers. The E^1_{2g} peak at 378 cm^{-1} and the A_{1g} one at 404 cm^{-1} show the opposite vibration of two S atoms with respect to the Mo atom and the out of plane opposite vibration of the S atoms in opposite directions, respectively. Compared to the 2H phase, 1T′-MoS_2 displays a slightly weaker E^1_{2g} band due to the existence of defects. Notably, there is no A_{1g} band present in 1T′ phase MoS_2 which indicates the weakened interactions between the adjacent layers because of the intercalated molecules with the MoS_2 layers (Fig. 1(a)).[32]

To better understand the electronic structure of as-prepared 2H- and 1T′-MoS_2, X-ray absorption near edge structure (XANES) spectroscopy was performed. Commercial 2H-MoS_2 was taken as the standard. The results (Fig. 2(a)) suggest that the oxidation state of Mo in both samples is +4 as the energy positions of the Mo K-edge are close to that of the commercial MoS_2 standard. However, the chemical state of Mo in 1T′-MoS_2 was a little lower than that of 2H-MoS_2 according to the spectra, which indicated that the surface of 1T′-MoS_2 is electron rich. The valence state and near-surface composition of 2H and 1T′ phases were further identified by X-ray photoelectron spectroscopy (XPS). All the spectra are calibrated using the C 1s peak at 284.8 eV. The energy shifts of the Mo (3d) and the S (2p) peaks further indicate the different electronic states of the 1T′ and 2H phases.[35] As shown in Fig. 2(c), two peaks of Mo^{4+} (3d) at around 229 and 232 eV correspond to binding energies of Mo^{4+} $3d_{5/2}$ and $3d_{3/2}$ electrons in 2H-MoS_2, respectively. In addition to these two peaks, a new doublet peak (228.4 and 231.6 eV) appeared for 1T′-MoS_2.[36] The Mo ($3d_{5/2}$) peak of the 1T′ phase shifted to a lower binding energy (0.88 eV) relative to that of 2H-MoS_2, showing the increasing electron density on 1T′-MoS_2, which is consistent with the XANES studies. By deconvoluting the Mo (3d) peak, it can be estimated that 80% of Mo is in the 1T′ phase in the as-prepared 1T′-MoS_2 samples. The S ($2p_{3/2}$) peak also showed a similar shift to Mo ($3d_{5/2}$) (Fig. 2(c)). Compared to the 2H phase with one S (2p) doublet with a binding energy of 162.6 eV, the hydrazine-intercalated 1T′ phase has an extra split S (2p) doublet peak at 161.3 eV. In addition, the XPS spectra of N (1s) are presented in Fig. S3. The peak at 399.4 eV can be ascribed to the characteristic signals of intercalated or adsorbed N_2H_4 species,[37] suggesting the occurrence of charge transfer from N to MoS_2. Importantly, the presence of N as an n-type dopant in MoS_2 can shift the Fermi level closer to the valence band, thereby facilitating charge transfer. This effect arises from band bending induced by the formation of Mo–N covalent bonds and the preferential removal of S atoms.[38,39] Besides, the XPS analysis based on the survey scan indicates that the atomic ratio of Mo to S atoms is approximately 1 : 1.86 for 2H-MoS_2 but decreased to 1 : 1.63 for 1T′-MoS_2, indicating an increased number of S vacancies in the 1T′ phase (Fig. S4 and Table S1).

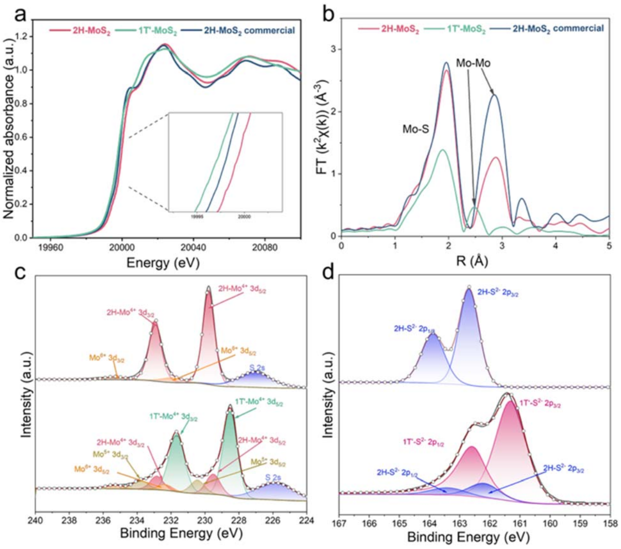

Fig. 2 (a) XANES spectra & (b) k^2-weighted Fourier transformed EXAFS spectra of the Mo K-edge of the as-prepared and standard MoS_2 samples; (c) Mo 3d XPS spectra & (d) S 2p XPS spectra of as prepared 2H- and 1T′-MoS_2.

Furthermore, the atomic coordination was investigated by extended X-ray absorption fine structure (EXAFS) spectroscopy. As shown in Fig. S5, the Mo K-edge oscillation curve of 1T′-MoS_2 differs significantly from those of 2H-MoS_2 and commercial MoS_2, indicating substantial changes in local atomic arrangements. These differences are further clarified by the Fourier Transform (FT) profiles in real space (Fig. 2(b)). For 2H-MoS_2, the FT curve features two main peaks at 1.96 Å and 2.85 Å, corresponding to the nearest Mo–S and Mo–Mo distances, respectively. In contrast, 1T′-MoS_2 exhibits a noticeable second peak at 2.48 Å instead of 2.85 Å in 2H-MoS_2, indicating a change in the Mo–Mo distance and the local structure changes. Additionally, the peak intensity of the Mo–S bond decreases for 1T′-MoS_2, likely due to defect formation induced by N_2H_4 intercalation, while the Mo–Mo peak intensity also decreased, suggesting a corresponding reduction in the coordination number. These observations may indicate a structural transformation in which one sulfur basal plane of 1T-MoS_2 rotates by 60° along the *c*-axis relative to the 2H-phase trigonal prismatic structure, resulting in a distorted octahedral coordination (1T′) (Fig. S6).[40] To obtain quantitative structural parameters, EXAFS fitting was conducted using ARTEMIS[41] software, with the results summarized in Table S2 and Fig. S7.

Optimal carbon ratio for the electrocatalytic NORR

Prior to the evaluation of the MoS_2 catalysts for the NORR in a PEM electrolyzer, the optimal ratio of mixing as-synthesized MoS_2 materials with electrically conducting carbon black was first investigated. Conductive carbon black is indispensable to drop-cast electrodes for ensuring smooth charge transfer at the catalyst interface and maximizing the utilization of the catalyst surface, especially for MoS_2 given its intrinsic semiconducting nature. The tests were first performed in a rotating disk electrode (RDE) setup, which allows for more precise control of mass transport, speeding up the investigation process compared to the multi-step preparation for testing in a PEM electrolyzer.[42] 2H-MoS_2 was used for this investigation, and the *iR*-corrected polarization curves in 0.1 M H_2SO_4 were used to compare performance with different relative carbon amounts. In the MoS_2/C (carbon black) composition, the loading of 2H-MoS_2 (1 mg cm^{-2}) was kept constant and the amount of carbon black was changed with respect to the total weight of 2H-MoS_2 from 100 wt% to 30 wt%, decreasing with a step of 10 wt%. The physically mixed 2H-MoS_2/C was drop-cast on a glassy carbon electrode in the RDE setup (see the Method section for a detailed description). The results are shown in Fig. S8. 50 wt% of Vulcan carbon black mixture exhibited the best electrochemical activity among all the mixing ratios, while a further increase in the amount of carbon black resulted in decreasing activity. Pure MoS_2 exhibited activity, but the performance was poor and lower than that of all the samples with carbon black mixing. Also, the electrochemical surface area (ECSA) was investigated by measuring the double-layer capacitance (C_{dl}) in the non-faradaic region. The results are shown in Fig. S9. Derived from cyclic voltammetry (CV) curves obtained at various scan rates, the C_{dl} value was the highest at 50 wt% carbon black mixture with 7.7 mF cm^{-2} and decreased with a higher amount of carbon black (Fig. S10).

The RDE results suggest that a physical mixture containing 50 wt% of carbon black would perform best, and therefore, pure MoS_2 and 40, 50 and 60 wt% of MoS_2 on carbon black were selected to test the NORR activity in a PEM electrolyzer. To better understand the relationship between the mass transfer limitation and reaction activity at a relatively low concentration of NO (5 vol% in He), different types of gas diffusion layers, namely a hydrophilic Ti GDL and hydrophobic carbon paper (Sargent 39BB), were investigated. Fig. 3(a) shows the FE towards different products during the NORR for (i) pure MoS_2 with a Ti GDL, (ii) pure MoS_2, and (iii) 40, (iv) 50 and (v) 60 wt% carbon black with carbon paper (CP, for (ii)–(v)) at 2.1 V, respectively. The FE in the full tested cell potential range (from 1.7–2.3 V) is shown in Fig. S11. Electrochemical NORR activity of only carbon black was also examined as a control experiment. Carbon black itself exhibits low total current density, intriguingly with a reasonable selectivity towards ammonia (Fig. S12).

Mainly H_2 was produced when using a Ti GDL, due to its hydrophilic character. A thin water layer could possibility form on the membrane surface because of the electro-osmosis process. This layer slows NO gas diffusion to the MoS_2 active sites and as NO has low solubility in water, the reaction undergoes to the HER instead of the NORR. Changing the gas diffusion layer to hydrophobic carbon paper improves the removal of the water layer formed during the reaction, promoting the desired NORR over the HER. Therefore, using carbon paper as a gas diffusion layer is the best combination for the NORR. From the study of the carbon ratio, product selectivity results also align with the previous RDE test results. Without a mixture of carbon, the HER is the dominant reaction (81.0% FE towards H_2) with zero FE_{NH_3}. The HER is suppressed by adding carbon black to the catalyst layer. FE_{NH_3} increases to 60.0% with 40 wt% carbon, while FE_{H_2} drops to less than 12.7% at 2.1 V. The undesired HER is suppressed with an increasing carbon ratio, with 40MoS_2/60C showing the lowest FE (less than 10%) towards H_2.

Notably, pure MoS_2 with a Ti GDL and carbon paper is more selective towards NH_2OH (Fig. S11(a and b)). NH_2OH is a reaction intermediate towards NH_3 production *via* a NO reduction process and has high solubility in water.[43] Water contact angle measurements were performed to check the hydrophobicity of the as prepared catalyst layer on the membrane. The results are shown in Fig. 3(c) and indicated that without an additional carbon mixture, the contact angle of the catalyst layer is 125°, which is a bit more hydrophilic compared to that when adding extra carbon black (150° with 50 wt% carbon black). Thus, we hypothesize that the water layer during the reaction or due to the electro-osmosis drag could not be removed efficiently, and therefore, the remaining water could potentially desorb NH_2OH from the active sites of MoS_2 and thus prevent further NH_3 formation. Carbon black can also improve the mass transport limitation of insoluble reactants which allows a dramatic reduction in the gas diffusion pathway, especially with low concentration NO. 50MoS_2/C displays the highest current density (78 mA cm^{-2}) and FE towards NH_3 (86% at 2.1 V), which indicates that not only more active sites but also more reactants are available for the reaction.

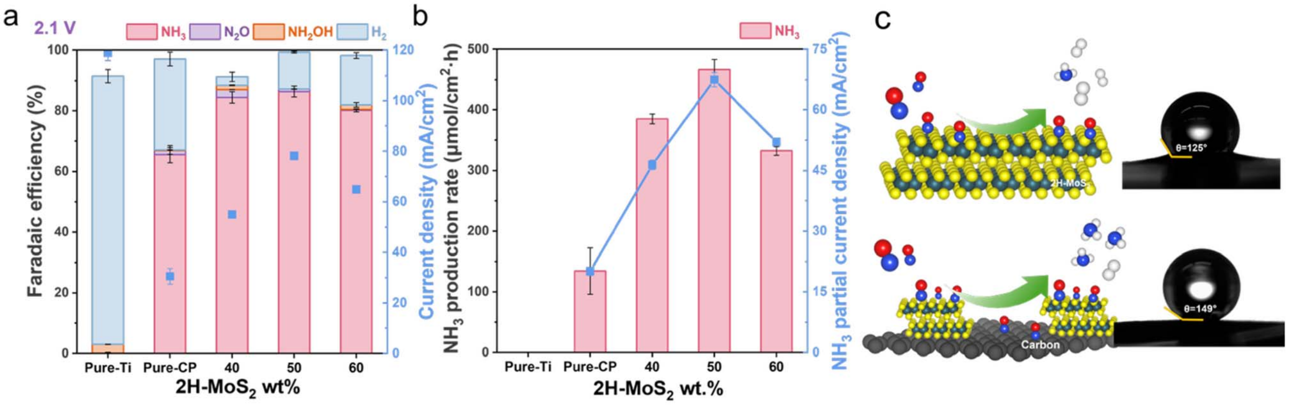

Fig. 3 (a) Faradaic efficiency & total current density; (b) ammonia production rate & partial current density of 2H-MoS_2 at no or different degrees of mixing with carbon black; (c) schematic illustrations and water-contact angle measurement of the enhanced NO mass transport.

The NH_3 production rate and partial current density results align with the previous results (Fig. 3(b)). 50MoS$_2$/C achieves an excellent performance of 466 μmol cm^{-2} h^{-1}, while pure MoS$_2$ produces only 134 μmol cm^{-2} h^{-1} ammonia at 2.1 V. The NH_3 yield of other studied configurations is shown in Fig. S13 and a comparison with the current literature is shown in Table S4. There is no NH_3 production using the Ti GDL and the ammonia production rate reached a plateau at a higher voltage which indicates that the HER takes over compared to the NORR. NH_3 partial current density follows the same trend as the ammonia production rate for all measurements. The single pass NO conversion rate is summarized in Fig. S14. A major advantage of conducting the NORR in a PEM electrolyzer is that it is suitable for continuous NO conversion, which is beneficial for scaled-up operations often required in the chemical industry. The enhanced performance by mixing with carbon black can be ascribed to the significant increase in the mass transport rate through the hydrophobic carbon layer, which can further compensate for the low concentration NO gas inlet, thereby inhibiting excess *H for H_2 generation. However, with an excess amount of carbon, the availability of active sides was hindered, and low catalytic activity was observed.

According to previous findings, a physical mixture with 50 wt% carbon black was used to compare the catalytic performance of the NORR between 2H- and 1T′-MoS$_2$. Electrochemical impedance spectroscopy (EIS) in Fig. 4(a) reveals that the 1T′ phase exhibits a significantly lower charge transfer resistance (R_{ct}) compared to the 2H phase. While R_{ct} primarily reflects the kinetic barrier for the reaction at the interface, this drastic reduction suggests that the semi-metallic character of the 1T′ phase facilitates rapid electron transfer to surface active sites. Furthermore, the lower ohmic cell resistance (R_s) observed in the 1T′ sample confirms the improved bulk electrical conductivity.

The reduction of NO to NH_4^+ is a 5-electron and 6-proton multistep reaction ($NO + 6H^+ + 5e^- \rightarrow NH_4^+ + H_2O$) and the N–N coupling is a critical step to detoxify NO to harmless dinitrogen. However, the NH_4^+ production in this reaction could compete with N–N coupling ($2NO + 4H^+ + 4e^- \rightarrow N_2 + 2H_2O$ & $2NO + 2H^+ + 2e^- \rightarrow N_2O + H_2O$). The faradaic efficiency and product selectivity of electrocatalytic NO reduction on 2H- and 1T′-MoS$_2$ at different cell potentials in the PEM electrolyzer are shown in Fig. 4(b and c). 2H-MoS$_2$ shows markedly higher selectivity toward ammonia than 1T′-MoS$_2$ over the entire cell-voltage range. As the cell voltage increases, FE_{NH_3} increases and reaches a maximum of 86% at 2.1 V with a current density of 78 mA cm^{-2}. The ammonia production rate also increases with cell potential, although the rate of increase becomes smaller at higher voltages, indicating that the additional current is diverted to the competing HER rather than to NO reduction (Fig. S15(a)). Consistently, at higher cell voltages FE_{NH_3} decreases while FE_{H_2} increases, confirming that the HER becomes increasingly dominant.

In contrast, 1T′-MoS$_2$ shows a lower NH_3 selectivity, with a FE_{NH_3} maximum of 48% at 1.9 V. Notably, 1T′-MoS$_2$ shows substantially higher N_2 selectivity at low cell voltage, reaching around 50% FE_{N_2} at 1.7 V, but this N_2 selectivity rapidly diminishes to <1% at 2.3 V. With increasing cell voltage, the product distribution on 1T′ shifts away from N_2 toward NH_3 and ultimately toward H_2, suggesting that the higher driving force

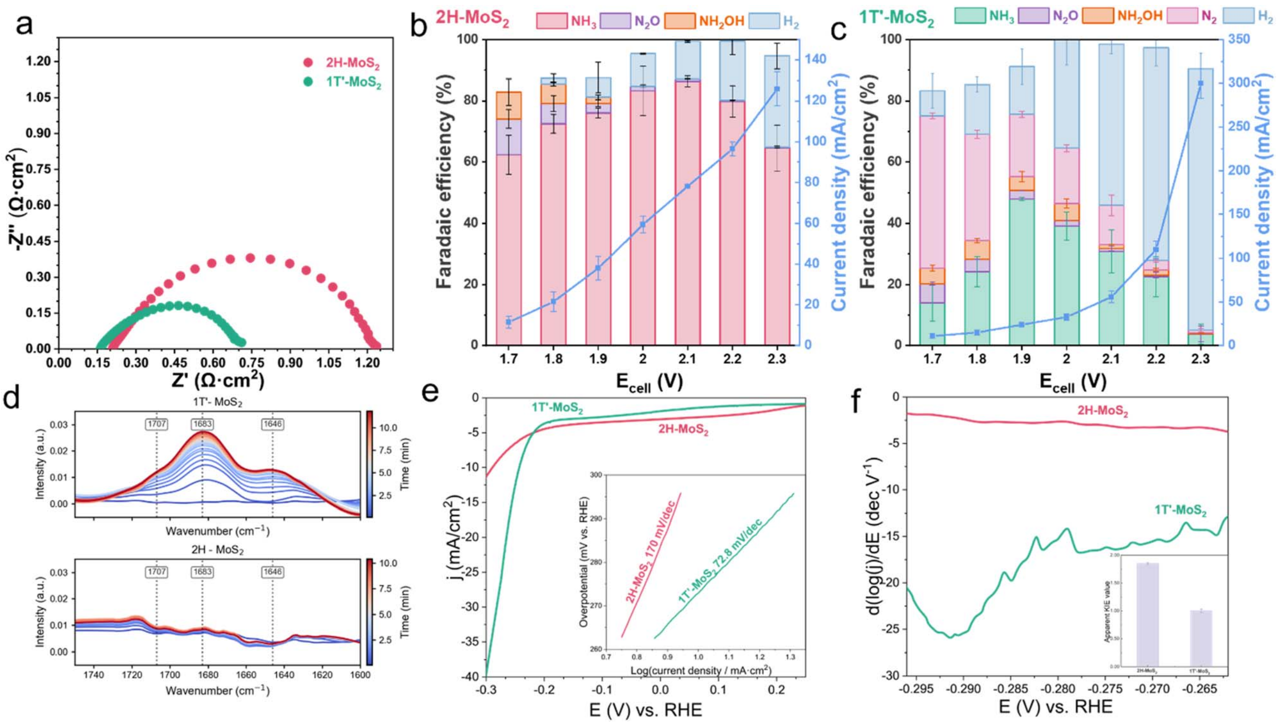

Fig. 4 (a) EIS measurement for 2H and 1T′ MoS$_2$; (b and c) faradaic efficiency and total current density for 2H and 1T′ phase MoS$_2$; (d) NO adsorption for 2H and 1T′ phase MoS$_2$; (e) LSV and Tafel slope; (f) local Tafel derivative and apparent KIE values for 2H and 1T′ phase MoS$_2$.

increasingly promotes proton-coupled processes and the HER that suppress the NORR. This is further supported by the decline in the NH_3 production rate and the decrease in NH_3 partial current density at the highest voltages, despite the increase in total current, highlighting that the additional current is largely consumed by the HER (Fig. S15(b)).

The single pass NO conversion rate of 2H- and 1T′-MoS_2 is presented in Fig. S15(c), 2H-MoS_2 exhibits higher NO conversion than 1T′-MoS_2, and reaches around 67% at 2.3 V which is 3.4 times higher than that of 1T′-MoS_2. One way to assess the accessibility of active sites in both catalysts is by comparing the pore size distribution of these materials. Thus, the specific surface area and porosity of the as-prepared 2H- and 1T′-MoS_2 were characterized *via* N_2 adsorption–desorption isotherms (Fig. S16). For 2H- and 1T′-MoS_2, the major pores size is centred at 4 nm, while 2H-MoS_2 shows few smaller and larger size distributions compared to 1T′-MoS_2. 2H-MoS_2 exhibited a specific surface area (SSA) of 33 $m^2\ g^{-1}$, which is approximately 3 times greater than that of 1T′-MoS_2 (13 $m^2\ g^{-1}$). The lower SSA of the 1T′ phase reflects this dense spherical aggregation, which limits the access of gas to the internal surfaces compared to the more open 2H morphology (Fig. 1(b and c)). Based on the above results, it implies that under electrocatalytic conditions, 2H-MoS_2 could offer more accessibility to the reactant NO, which is beneficial especially in low concentration NO feed.

Our experimental results show that two different phases of MoS_2 display markedly different NORR selectivity, with 1T′ favoring N_2 formation and 2H favoring NH_3 formation. To rationalize this difference, we have performed kinetics study and *ex situ* diffuse reflectance infrared Fourier transform spectroscopy (DRIFTS) measurements. As shown in Fig. 4(d and e), 2H-MoS_2 does not show a clear growth of distinct NO-related adsorption bands and is dominated by a water signal, whereas 1T′-MoS_2 displays a pronounced NO adsorption peak. The intensity of the signal at 1683 cm^{-1}, which corresponds to the coupled mononitrosyl or dinitrosyl adsorption,[44] increased substantially. These results also indicate that the 1T′ phase has high surface coverage of NO compared to that of the 2H phase, which can promote the N–N coupling.

To compare kinetics on a consistent basis, we evaluate the local Tafel/derivative behavior and the apparent NORR kinetic isotope effect (apparent KIE)[45] within the same potential window (−0.262 V to −0.296 V *vs.* RHE). The determination decision of the potential is shown in Fig. S17. 2H exhibits a flatter and more stable $d(\log|j|)/dE$ response, whereas 1T′ shows a much steeper (more potential-sensitive) derivative, indicating different apparent rate-control characteristics. Importantly, the isotope response in the same window reveals a pronounced apparent KIE for 2H (∼1.85) but an approximately unity KIE for 1T′ (Fig. S18). The strong isotope sensitivity on 2H suggests that proton-involving sub-steps contribute substantially to the overall rate in this regime,[46] consistent with enhanced NH_3 selectivity, while the near-unity KIE on 1T′ indicates that the dominant current-determining step is comparatively H/D-insensitive.

Taken together, 1T′ stabilizes NO-derived adsorbates more strongly, enabling higher NO* coverage and facilitating N-N coupling routes toward N_2, while 2H proceeds *via* a more proton-coupled hydrogenation pathway that correlates with enhanced NH_3 selectivity.[47]

The metallic phase 1T′-MoS_2 is known to be metastable with higher ground-state energy than the semiconducting 2H-MoS_2. Consequently, it can undergo phase transformation to the 2H structure during reactions.[48,49] *Ex situ* XPS is performed to clarify the stability of both 2H- and 1T′-MoS_2 after the NORR (Fig. 5(a–d)). For 1T′-MoS_2, the XPS results indicate a reduction in the 1T′ phase after the reaction, accompanied by a pronounced increase in the 2H phase and Mo(V)/Mo(VI) species. This suggests the transformation of unstable Mo species into more thermodynamically stable forms. In comparison, 2H-MoS_2 exhibits similar changes in the Mo 3d spectra but with greater structural stability following the reaction. The relative atomic ratio of different Mo species is shown in Table S3. The results reveal a significant increase in Mo(V) and Mo(VI) compounds in 1T′-MoS_2-from 5% to 56% after the reaction. This substantial increase implies that more Mo(V) species were formed during the reaction, which were subsequently oxidized to Mo(VI), likely due to exposure to NO, air, or H_2O.[50,51] These findings corroborate the enhanced formation of N–N coupling products observed for 1T′-MoS_2, highlighting Mo(V) as a key intermediate in the reaction pathway. Notably, the S 2p spectra show an additional spin–orbit doublet (at 163.6 and 164.8 eV) in both MoS_2 phases after the reaction, relative to their fresh counterparts. This signal is attributed to $(S_2)^{2-}$ species, commonly found in amorphous sulfur-rich MoS_3, indicating the possible formation of $MoOS_2$ during the reaction process.[52–54] The 1T′-MoS_2 sample shows a higher abundance of $(S_2)^{2-}$ species compared to 2H-MoS_2, which is consistent with the corresponding Mo 3d spectra. These bridging disulfide species $(S_2)^{2-}$ serve as active protonation sites, potentially enhancing the hydrogen evolution reaction (HER), particularly at higher applied voltages.[55,56]

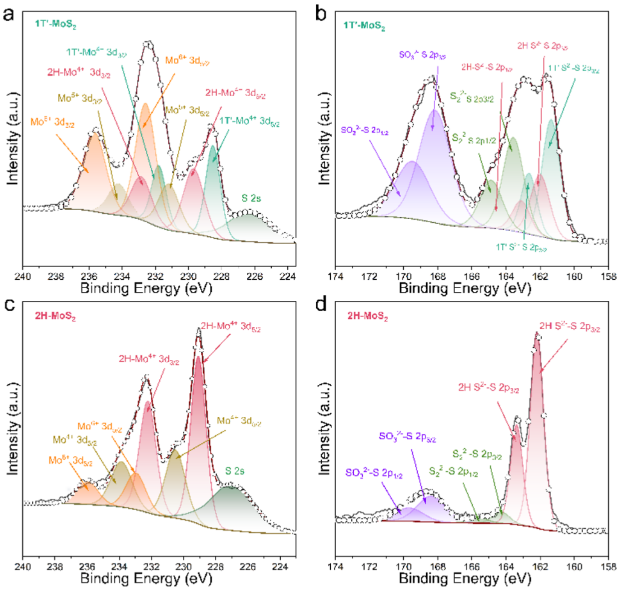

Fig. 5 (a and c) Mo 3d XPS spectra; (b and d) S 2p XPS spectra of 2H and 1T′ phase MoS_2 after the reaction.

Conclusion

In conclusion, our study explores 2H and 1T′ phases of MoS_2 and their effects on activity and selectivity towards multi-step proton–electron transfer electrocatalytic NO reduction. Through different carbon mixture experiments and testing different gas diffusion layer materials, we identified that the hydrophobicity of the catalyst layer enhances the adsorption of NO and improved the NO coverage on the catalyst surface, thus promoting NO reduction especially in low NO concentration steam. The optimal physical carbon mixture ratio of 50 wt% led to high FE towards NH_3 and a low HER rate. By regulating different crystal phases of MoS_2 (2H and 1T′), the selectivity of products significantly changed from NH_3 to N_2. 2H exhibits a large apparent KIE (~1.85) while 1T′ remains near unity, together with distinct local Tafel/derivative signatures, indicating fundamentally different apparent rate-control characteristics and a stronger proton-coupled contribution on 2H. Additionally, for 2H-MoS_2, a 67% single-pass NO conversion rate and 558 μmol cm^{-2} h^{-1} ammonia production rate were achieved at 2.3 V. Our investigation showed that electrocatalytic selectivity of MoS_2 or other transition metal dichalcogenides can be markedly regulated by phase engineering, and utilizing the sequential proton–electron transfer pathways could change the selectivity of complex multistep reactions. Our work could inspire future NORR electrocatalyst design, which could be further expanded to other complex multistep reactions like electrochemical CO/CO_2 reduction.

Experimental section

Chemicals and materials

Thiourea ($SC(NH_2)_2$), ammonium hepta-molybdate tetrahydrate ($(NH_4)_6Mo_7O_{24}\cdot 4H_2O$), hydrazine monohydrate ($N_2H_4\cdot H_2O$), hydrogen peroxide (H_2O_2), sulfuric acid (H_2SO_4), potassium iodate (KIO_3), hydrolymine (NH_2OH) and neutral red were purchased from Sigma Aldrich. Iridium(IV) oxide Premion™ (IrO_2) 99.99% was purchased from Therma Scientific Chemicals. Vulcan XC72 carbon black was bought from Cabot Corporation. Nafion™ 115 membranes were procured from Ion power, porous sintered titanium gas diffusion layers were purchased from Bekaert, and the carbon gas diffusion layer (GDL) Sigracet 39 BB was from Fuel Cell Store.

Preparation of 2H-MoS_2 nanosheets

2H-MoS_2 was synthesized using the hydrothermal method. Briefly, 0.53 g (0.4 mmol) of $(NH_4)_6Mo_7O_{24}\cdot 4H_2O$ and 1.83 g (24 mmol) of $SC(NH_2)_2$ were dissolved in 30 mL of MilliQ water and stirred to form a homogeneous solution. After that, the solution was transferred to a 45 mL stainless-steel autoclave with a polyparaphenol (PPL) liner and heated to 220 °C for 12 hours. After cooling down naturally to room temperature, the products were extracted, filtered and washed with water and ethanol 6 times. The obtained catalyst powder was dried in a vacuum oven at 60 °C for 12 hours.

Preparation of 1T′-MoS_2 nanosheets

1T′ phase dominated MoS_2 was synthesized by the one-step hydrazine assisted hydrothermal method which is modified based on the 2H-MoS_2 method described previously. Additionally, 0.29 mL (6 mmol) of $N_2H_4\cdot H_2O$ with a molar ratio of N_2H_4/Mo of 2 : 1 was added into the solution. The synthesis was completed at 180 °C for 10 hours and rapidly cooled down to room temperature. The rest remained the same as in the synthesis of 2H-MoS_2 samples.

Materials characterization

Powder X-ray diffraction (XRD) was recorded using a Bruker D8 ADVANCE X-ray diffractometer with a Cu Kα radiation source in the range of 5° to 90° with a step of 0.05°. The surface morphology of the catalysts was characterized by scanning electron microscopy (SEM). Raman spectra were recorded from 500 to 3000 cm^{-1} on a Horiba Scientific LabRAM HR Evolution Raman Spectroscopy system with an excitation wavelength of 514 nm. The composition and chemical bonding were analyzed by using a Thermo Scientific Kα system with Al Kα radiation (1486.7 eV). All binding energies for XPS spectra were calibrated according to the C 1s peak at 284.8 eV. Contact angle measurements were performed *via* a sessile drop using an OCA 25 goniometer (Dataphysics instruments Gmbh, Filderstadt, Germany), and 2 μL of droplets were dispensed onto substrates using an automatic pipetting unit. Measurements were conducted in ambient air with a temperature in the range of 20–24 °C. Specific surface areas were determined by the Brunauer–Emmett–Teller (BET) method. The Mo K-edge X-ray absorption near-edge (XANES) spectra and X-ray absorption fine structure (EXAFS) spectra were measured at the BL16-NOTOS beamline of the ALBA Synchrotron, Spain.

Electrode preparation

Nafion™ 115 membranes (3 × 3 cm^2) were pre-treated according to the procedure of 1 hour in 5 wt% hydrogen peroxide (H_2O_2) solution and 1 hour in 0.5 M H_2SO_4 solution at 80 °C and 1 hour in boiling MilliQ water. 4 mg of commercial IrO_2 (1 mg cm^{-2}) with 20 wt% Nafion ionomers were ultrasonically dispersed in 1 mL isopropanol and water (volume ratio: 50 : 50) for 1 hour to get a homogeneous ink. The cathodic ink was prepared in the same way with as prepared 2H-MoS_2 or 1T′-MoS_2, Vulcan XC72 carbon black (from 10 wt% to 70 wt%) and 30 wt% Nafion ionomers, while maintaining a constant 2H-MoS_2 loading of 1 mg cm^{-2} for the carbon black ratio optimization experiments. For 1T′-MoS_2, catalyst ink was prepared by adding 50 wt% of carbon black and 30 wt% Nafion ionomer. The ink was then spray-coated onto an membrane with a 2 × 2 cm^2 active geometry area. The catalyst inks were finally sprayed at 60 °C onto both sides of membranes using an automatic spray coater (CNC Airbrush Singular). After spray coating, the membrane was hot-pressed at 120 °C and 1 tonne for 3 minutes.

Electrochemical NO reduction test

The electrochemical NO reduction experiments were conducted in the PEM electrolyser (Fig. S19) on an AUTOLAB PGSTAT302N potentiostat equipped with a 20 A booster. The PEM electrolyser was operating at 80 °C. For electrochemical NO reduction, in the cathode chamber, the mixture of 5% NO and 4% CH_4 in He flowed at 27 mL min^{-1}. CH_4 was acting as the internal standard to correct the volume changes during reactions. In the anode chamber, MilliQ water was supplied at a flow rate of 1 mL min^{-1} by using a peristaltic pump (Ismatec). After the reaction, the cathode chamber outlet was connected to an acid trap with 0.1 M H_2SO_4 solution to trap the produced ammonia (NH_3) and hydrolymine (NH_2OH). After the acid trap, the gas flowed to the connected Bruker ALPHA infrared spectrometer and gas chromatograph (GC). The reactions were carried out at constant potential in the range of 1.7 V to 2.3 V for 30 minutes each. Electrochemical impedance spectroscopy (EIS) was conducted at the catalytically relevant potential of 1.7 V over a frequency range of 100 kHz to 0.1 Hz, using 10 points per decade and an AC perturbation amplitude of 10 mV.

Production quantification

The gaseous NO reduction products nitrous oxide (N_2O) and unreacted NO, and external standard CH_4 were analysed by using a Bruker Alpha infrared spectrometer. N_2 and H_2 were analysed by using a CompactGC (Global Analyser Solutions) equipped with a thermal conductivity detector (TCD). Ammonium (NH_4^+) collected at the acid trap was quantified using an ion chromatograph (IC, Metrohm 883 Basic ion chromatography), equipped with a Metrosep C6 separation column. Hydroxylamine (NH_2OH) was quantified by UV-vis spectroscopy (Unicam UV 500), measuring absorbance at 525 nm. The procedure consists of adding 1 mL of the sample with 5 mL of MilliQ water, 1 mL of 0.047 mol per L KIO_3 and 1 mL of 3 M H_2SO_4, 2 mL of neutral red is added after 5 minutes. The calibration curve of the natural red method for quantifying NH_2OH is shown in Fig. S20.

RDE measurements

Cyclic voltammetry (CV) and linear scan voltammetry (LSV) were conducted using a three-electrode electrochemical glass cell (graphene rod as the counter and Ag/AgCl as the reference electrodes) at room temperature with argon and NO purging. A glassy carbon disc of 0.196 cm^2 (5 mm diameter) was used as the working electrode in rotating disk electrode measurements (RDE, Pine Instruments). 15 μL of catalyst ink (details described in the previous section) was loaded onto the glassy carbon electrode for all the measurements in 100 mL of freshly prepared 0.1 M H_2SO_4 solution. Prior to the measurements, the electrode was electrochemically cleaned by repetitive potential scans between −0.4 V and 0.8 V *vs.* RHE until a stable cyclic voltammogram was obtained. All potentials were converted into the reversible hydrogen electrode (RHE) scale, and 85% *iR* corrections were applied to all results. The apparent NORR kinetic isotope effect was measured in a batch type H-cell in 0.1 M H_2SO_4 electrolyte and 0.1 M D_2SO_4 with NO saturation. For D_2O-based electrolytes, the apparent pD was calculated from the H_2O-calibrated pH meter reading according to $pD = pH + 0.4$.

Author contributions

M. L. and A. U. conceived the project. M. L. led experiments, data analysis, and figure design. F. H. B. assisted with electrochemical testing and scientific discussion. B. L. assisted with Raman measurement. M. C. assisted with electrochemical testing in the RDE set-up. S. M. assisted with X-ray absorption measurement. R. K. assisted with scientific discussion. A. U. assisted with project supervision and scientific discussion. M. L. and A. U. wrote the manuscript with editing contributions from all the authors.

Conflicts of interest

The authors declare no competing interests.

Data availability

The data supporting this article have been included as part of the supplementary information (SI). The authors will upload the figure data on a repository once they are finalised. Supplementary information: further characterization data of as synthesized MoS_2 catalysts (XPS, EXAFS fitting data, and BET) and electrochemical test data. See DOI: https://doi.org/10.1039/d5ta09769j.

Acknowledgements

M. L. acknowledges funding from the China Scholarship Council. The authors are grateful to ALBA synchrotron for beamtime at the NOTOS beamline (proposal number: 2024098746).

References

1 J. I. Sprent, *The Ecology of the Nitrogen Cycle*, Cambridge University Press, 1987.
2 V. Rosca, M. Duca, M. T. de Groot and M. T. M. Koper, *Chem. Rev.*, 2009, **109**, 2209–2244.
3 J. Leverett, W. H. Lie, M. H. A. Khan, Z. Ma, R. Daiyan and R. Amal, *Sustainable Energy Fuels*, 2025, **9**, 3780–3790.
4 L. Alves, L. I. V. Holz, C. Fernandes, P. Ribeirinha, D. Mendes, D. P. Fagg and A. Mendes, *Renewable Sustainable Energy Rev.*, 2022, **155**, 111916.
5 M. Okubo and T. Kuwahara, in *New Technologies for Emission Control in Marine Diesel Engines*, ed. M. Okubo and T. Kuwahara, Butterworth-Heinemann, 2020, pp. 53–143.
6 V. Praveena and M. L. J. Martin, *J. Energy Inst.*, 2018, **91**, 704–720.
7 M. Pinzón, R. García-Carpintero, A. R. de la Osa, A. Romero, D. Abad-Correa and P. Sánchez, *Energy Convers. Manage.*, 2024, **321**, 118998.
8 M. Van Damme, L. Clarisse, S. Whitburn, J. Hadji-Lazaro, D. Hurtmans, C. Clerbaux and P.-F. Coheur, *Nature*, 2018, **564**, 99–103.
9 J. Humphreys, R. Lan and S. Tao, *Adv. Energy Sustainability Res.*, 2021, **2**, 2000043.

10 J. Long, S. Chen, Y. Zhang, C. Guo, X. Fu, D. Deng and J. Xiao, *Angew. Chem., Int. Ed.*, 2020, **59**, 9711–9718.

11 Y.-w. Wu, H.-w. Wang, Z.-l. Wu, X. Zhang, Y. Dong, Z. Hu, Y. Lv, X.-y. Zhou, L. Zhao, B. Zhang and Q. Lu, *Sep. Purif. Technol.*, 2025, **366**, 132813.

12 J. H. Montoya, C. Tsai, A. Vojvodic and J. K. Nørskov, *ChemSusChem*, 2015, **8**, 2180–2186.

13 B. H. Ko, B. Hasa, H. Shin, Y. Zhao and F. Jiao, *J. Am. Chem. Soc.*, 2022, **144**, 1258–1266.

14 H. Wan, A. Bagger and J. Rossmeisl, *Angew. Chem., Int. Ed.*, 2021, **60**, 21966–21972.

15 R. Sander, *Atmos. Chem. Phys.*, 2023, **23**, 10901–12440.

16 S. Bunea, M. Coppens and A. Urakawa, *ACS Catal.*, 2023, **13**, 11345–11351.

17 M. Li, J. Verkuil, S. Bunea, R. Kortlever and A. Urakawa, *ChemSusChem*, 2023, **16**, e202300949.

18 W. Yang, H. Liu, X. Chang, Y. Zhang, Y. Cai, Y. Li, Y. Cui, B. Xu, L. Yu, X. Cui and D. Deng, *Nat. Commun.*, 2025, **16**, 1257.

19 A. C. A. de Vooys, M. T. M. Koper, R. A. van Santen and J. A. R. van Veen, *Electrochim. Acta*, 2001, **46**, 923–930.

20 Z. Wang, H. Duan, W. Qu, H. Zhang, L. Han, Z. Teng, G. Chen, D. Cheng, X. Wang, Y. A. Wu, M. Xie and D. Zhang, *Adv. Funct. Mater.*, 2025, **35**, 2507533.

21 J. Meng, C. Cheng, Y. Wang, Y. Yu and B. Zhang, *J. Am. Chem. Soc.*, 2024, **146**, 10044–10051.

22 H. Chen, Y. Gao, J. Du, R. Hao, X. Wu, L. Wang and Z. Wu, *ACS Nano*, 2026, **20**, 2323–2336.

23 J. Theerthagiri, K. Karuppasamy, A. H. Mahadi, C. J. Moon, N. Rahamathulla, S. Kheawhom, S. Alameri, A. Alfantazi, A. P. Murthy and M. Y. Choi, *Environ. Chem. Lett.*, 2024, **22**, 189–208.

24 A. Mukherjee, N. Ojha, K. K. Pant, A. Deb, M. Abdinejad, S. S. Mahapatra and B. C. Ruidas, *Environ. Sci. Technol. Lett.*, 2025, **12**, 1113–1138.

25 W. Zhai, Z. Li, Y. Wang, L. Zhai, Y. Yao, S. Li, L. Wang, H. Yang, B. Chi, J. Liang, Z. Shi, Y. Ge, Z. Lai, Q. Yun, A. Zhang, Z. Wu, Q. He, B. Chen, Z. Huang and H. Zhang, *Chem. Rev.*, 2024, **124**, 4479–4539.

26 Y. Liu, M. Tursun, G. Hu, A. Abdukayum and C. Wu, *RSC Adv.*, 2025, **15**, 29323–29334.

27 D. He, H. Ooka, Y. Kim, Y. Li, F. Jin, S. H. Kim and R. Nakamura, *Proc. Natl. Acad. Sci. U. S. A.*, 2020, **117**, 31631–31638.

28 Y. Wang, Y. Xu, C. Cheng, B. Zhang, B. Zhang and Y. Yu, *Angew. Chem.*, 2024, **136**, e202315109.

29 M. Li, Z. Zhou, L. Hu, S. Wang, Y. Zhou, R. Zhu, X. Chu, A. Vinu, T. Wan, C. Cazorla, J. Yi and D. Chu, *ACS Appl. Mater. Interfaces*, 2022, **14**, 16338–16347.

30 M. Acerce, D. Voiry and M. Chhowalla, *Nat. Nanotechnol.*, 2015, **10**, 313–318.

31 J. Zheng, H. Zhang, S. Dong, Y. Liu, C. Tai Nai, H. Suk Shin, H. Young Jeong, B. Liu and K. Ping Loh, *Nat. Commun.*, 2014, **5**, 2995.

32 M. Li, D. Wang, J. Li, Z. Pan, H. Ma, Y. Jiang and Z. Tian, *RSC Adv.*, 2016, **6**, 71534–71542.

33 K. Wu, X. Cao, M. Li, B. Lei, J. Zhan and M. Wu, *Small*, 2020, **16**, 2006532.

34 J. Xie, H. Zhang, S. Li, R. Wang, X. Sun, M. Zhou, J. Zhou, X. W. Lou and Y. Xie, *Adv. Mater.*, 2013, **25**, 5807–5813.

35 X. Fan, P. Xu, D. Zhou, Y. Sun, Y. C. Li, M. A. T. Nguyen, M. Terrones and T. E. Mallouk, *Nano Lett.*, 2015, **15**, 5956–5960.

36 L. Cai, J. He, Q. Liu, T. Yao, L. Chen, W. Yan, F. Hu, Y. Jiang, Y. Zhao, T. Hu, Z. Sun and S. Wei, *J. Am. Chem. Soc.*, 2015, **137**, 2622–2627.

37 Z. Liu, J. Ou, H. Wang, X. You and M. Ye, *ACS Appl. Mater. Interfaces*, 2016, **8**, 32060–32067.

38 L. Feng, L. Zhang, S. Zhang, X. Chen, P. Li, Y. Gao, S. Xie, A. Zhang and H. Wang, *ACS Appl. Mater. Interfaces*, 2020, **12**, 17547–17556.

39 A. Azcatl, X. Qin, A. Prakash, C. Zhang, L. Cheng, Q. Wang, N. Lu, M. J. Kim, J. Kim, K. Cho, R. Addou, C. L. Hinkle, J. Appenzeller and R. M. Wallace, *Nano Lett.*, 2016, **16**, 5437–5443.

40 Q. Liu, X. Li, Q. He, A. Khalil, D. Liu, T. Xiang, X. Wu and L. Song, *Small*, 2015, **11**, 5556–5564.

41 H. Husain, M. Sulthonul, B. Hariyanto, C. Cholsuk and S. Pratapa, *Mater. Today: Proc.*, 2021, **44**, 3296–3300.

42 S. Nösberger, J. Du, J. Quinson, E. Berner, A. Zana, G. K. H. Wiberg and M. Arenz, *Electrochem. Sci. Adv.*, 2023, **3**, e2100190.

43 S. Garcia-Segura, M. Lanzarini-Lopes, K. Hristovski and P. Westerhoff, *Appl. Catal., B*, 2018, **236**, 546–568.

44 L. van Haandel, E. J. M. Hensen and T. Weber, *Catal. Today*, 2017, **292**, 67–73.

45 X. Gao, X.-Y. Yu and C.-R. Chang, *Phys. Chem. Chem. Phys.*, 2022, **24**, 15182–15194.

46 S. Hammes-Schiffer, *Acc. Chem. Res.*, 2025, **58**, 1335–1344.

47 D. He, H. Ooka, Y. Li, Y. Kim, A. Yamaguchi, K. Adachi, D. Hashizume, N. Yoshida, S. Toyoda, S. H. Kim and R. Nakamura, *Nat. Catal.*, 2022, **5**, 798–806.

48 K.-A. N. Duerloo, Y. Li and E. J. Reed, *Nat. Commun.*, 2014, **5**, 4214.

49 J. Heising and M. G. Kanatzidis, *J. Am. Chem. Soc.*, 1999, **121**, 638–643.

50 X. Zhang, F. Jia, B. Yang and S. Song, *J. Phys. Chem. C*, 2017, **121**, 9938–9943.

51 H. Li, S. Chen, Y. Zhang, Q. Zhang, X. Jia, Q. Zhang, L. Gu, X. Sun, L. Song and X. Wang, *Nat. Commun.*, 2018, **9**, 2452.

52 L. Benoist, D. Gonbeau, G. Pfister-Guillouzo, E. Schmidt, G. Meunier and A. Levasseur, *Thin Solid Films*, 1995, **258**, 110–114.

53 J. C. Dupin, D. Gonbeau, I. Martin-Litas, P. Vinatier and A. Levasseur, *Appl. Surf. Sci.*, 2001, **173**, 140–150.

54 D. Ryaboshapka and P. Afanasiev, *J. Catal.*, 2023, **426**, 30–38.

55 P. D. Tran, T. V. Tran, M. Orio, S. Torelli, Q. D. Truong, K. Nayuki, Y. Sasaki, S. Y. Chiam, R. Yi, I. Honma, J. Barber and V. Artero, *Nat. Mater.*, 2016, **15**, 640–646.

56 K. T. Santos, L. A. Z. Sanchez, V. Martin, F. Guillet, K. Kumar, X. Portier, F. Maillard, L. Oliviero and L. Dubau, *Electrochim. Acta*, 2024, **507**, 145195.